Article

Structure

High-resolution crystal structures of transient intermediates in the phytochrome photocycle

Graphical abstract

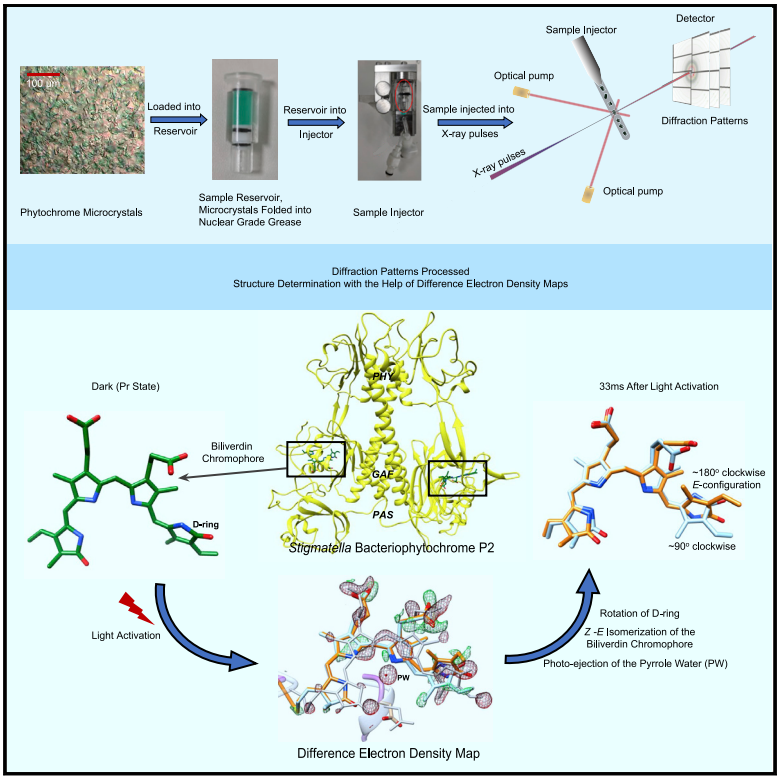

Highlights

- Successful TR-SFX experiments were conducted on a myxobacterial phytochrome at SACLA
- The *Z*-to-*E* isomerization of the biliverdin chromophore is observed at 5 ns and 33 ms
- Structural changes extend through the entire phytochrome at both time delays

Authors

Melissa Carrillo, Suraj Pandey, Juan Sanchez, ..., Sebastian Westenhoff, Emina A. Stojković, Marius Schmidt

Correspondence

sebastian.westenhoff.2@gu.se (S.W.), e-stojkovic@neiu.edu (E.A.S.), smarius@uwm.edu (M.S.)

In brief

Phytochromes are the molecular eyes of plants and bacteria that regulate cellular response to light, an essential environmental signal. Carrillo, Pandey et al. successfully investigate these structural changes in real time and with extreme magnification at one of the strongest X-ray sources, the free electron laser SACLA in Japan.

Carrillo et al., 2021, Structure *29*, 743–754
July 1, 2021
https://doi.org/10.1016/j.str.2021.03.004

CellPress

Structure

CellPress

Article

High-resolution crystal structures of transient intermediates in the phytochrome photocycle

Melissa Carrillo,[1,9] Suraj Pandey,[2,9] Juan Sanchez,[1] Moraima Noda,[1] Ishwor Poudyal,[2] Luis Aldama,[1] Tek Narsingh Malla,[2] Elin Claesson,[3] Weixiao Yuan Wahlgren,[3] Denisse Feliz,[1] Vukica Šrajer,[4] Michał Maj,[3] Leticia Castillon,[3] So Iwata,[5,6] Eriko Nango,[6,7] Rie Tanaka,[5,6] Tomoyuki Tanaka,[5,6] Luo Fangjia,[5,6] Kensuke Tono,[6,8] Shigeki Owada,[6,8] Sebastian Westenhoff,[3,*] Emina A. Stojković,[1,*] and Marius Schmidt[2,10,*]

[1]Department of Biology, Northeastern Illinois University, 5500 North St. Louis Avenue, Chicago, IL 60625, USA
[2]Physics Department, University of Wisconsin-Milwaukee, 3135 North Maryland Avenue, Milwaukee, WI 53211, USA
[3]Department of Chemistry and Molecular Biology, University of Gothenburg, Box 462, 40530 Gothenburg, Sweden
[4]The University of Chicago, Center for Advanced Radiation Sources, 9700 South Cass Avenue, Bldg 434B, Argonne, IL 60439, USA
[5]Department of Cell Biology, Graduate School of Medicine, Kyoto University, Yoshidakonoe-cho, Sakyo-ku, Kyoto 606-8501, Japan
[6]RIKEN SPring-8 Center, 1-1-1, Kouto, Sayo-cho, Sayo-gun, Hyogo 679-5148, Japan
[7]Institute of Multidisciplinary Research for Advanced Materials, Tohoku University, 2-1-1 Katahira, Aoba-ku, Sendai 980-8577, Japan
[8]Japan Synchrotron Radiation Research Institute, 1-1-1 Kouto, Sayo-cho, Sayo-gun, Hyogo 679-5198, Japan
[9]These authors contributed equally
[10]Lead contact
*Correspondence: sebastian.westenhoff.2@gu.se (S.W.), e-stojkovic@neiu.edu (E.A.S.), smarius@uwm.edu (M.S.)
https://doi.org/10.1016/j.str.2021.03.004

SUMMARY

Phytochromes are red/far-red light photoreceptors in bacteria to plants, which elicit a variety of important physiological responses. They display a reversible photocycle between the resting Pr state and the light-activated Pfr state. Light signals are transduced as structural change through the entire protein to modulate its activity. It is unknown how the Pr-to-Pfr interconversion occurs, as the structure of intermediates remains notoriously elusive. Here, we present short-lived crystal structures of the photosensory core modules of the bacteriophytochrome from myxobacterium *Stigmatella aurantiaca* captured by an X-ray free electron laser 5 ns and 33 ms after light illumination of the Pr state. We observe large structural displacements of the covalently bound bilin chromophore, which trigger a bifurcated signaling pathway that extends through the entire protein. The snapshots show with atomic precision how the signal progresses from the chromophore, explaining how plants, bacteria, and fungi sense red light.

INTRODUCTION

Phytochromes are red-light protein photoreceptors, initially discovered in plants (Butler et al., 1959) where they regulate essential physiological responses such as shade avoidance and etiolation (Batschauer, 1998), with which they are critical to the thriving of all vegetation on earth. Homologous proteins exist in bacteria (Davis et al., 1999; Jiang et al., 1999), cyanobacteria (Hughes et al., 1997; Yeh et al., 1997), and fungi (Blumenstein et al., 2005). In photosynthetic bacteria, they regulate the synthesis of light-harvesting complexes (Fixen et al., 2014; Giraud et al., 2002; Toh et al., 2011a; Yang et al., 2007, 2015). In non-photosynthetic bacteria their role is less understood, but they are involved in various processes such as the regulation of carotenoid pigments, which protect from harmful light exposure (Davis et al., 1999), in conjugation (Bai et al., 2016), plant colonization (McGrane and Beattie, 2017), quorum sensing, and multicellular fruiting body formation (Barkovits et al., 2011; Woitowich et al., 2018). Bacteriophytochromes (BphPs) have also been successfully used as infrared fluorescent tissue markers in mammals (Shu et al., 2009).

Phytochromes consist of two modules, where the N-terminal photosensory core module (PCM) is attached to a C-terminal effector module (Figure 1A) (Auldridge and Forest, 2011). The latter module provides enzymatic activity (Legris et al., 2019). At least in plant phytochromes, a stretch of amino acids at the N terminus is also functionally important (Cherry et al., 1992). BphPs are grouped into three classes according to the domain structure of their PCM (Auldridge and Forest, 2011). In plant and class I BphPs, the PCM consists of three domains called PAS (Per-ARNT-Sim), GAF (cGMP phosphodiesterase/adenylate cyclase/FhlA), and PHY (phytochrome-specific) (Takala et al., 2020) (Figures 1B and 1C). The module is conserved from bacteria to plants and holds a covalently bound bilin chromophore, an open-chain tetrapyrrole, which is biliverdin IXα (BV) in bacteria (Figure 2B). Hallmark features are: (1) a conserved

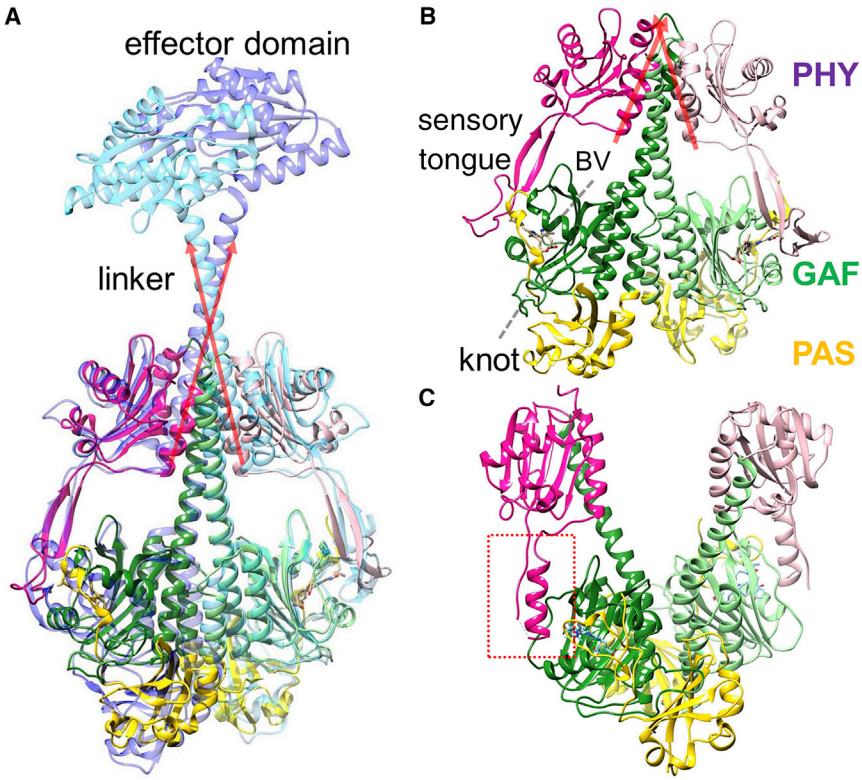

Figure 1. Bacteriophytochrome domain composition

PAS, GAF, and PHY domains are displayed in yellow, green, and magenta, respectively.

(A) The *Sa*BphP2 PCM structure in the Pr state is superposed over that of the intact (full-length) BphP from *Idiomarina* species (Gourinchas et al., 2017). The long red arrows denote the directions of the short C-terminal helices of the PHY domain and the linkers. The effector domain has diguanylyl cyclase activity, which is lightly regulated.

(B) The *Sa*BphP2 PCM structure in the Pr state. The directions of the short C-terminal helices are shown by red arrows. The biliverdin (BV) chromophore, the characteristic knot, and the sensory tongue are indicated.

(C) the (static) *Dr*BphP PCM structure in the Pfr state (Takala et al., 2014). The sensory tongue of the PHY domain is highlighted by the red dashed box.

water molecule, which is in contact with three of the four nitrogens of the BV and the backbone oxygen of a strictly conserved aspartic acid, called the pyrrole water (PW) (Wagner et al., 2005); (2) the so-called PHY (sensory) tongue, which changes fold in the Pr-to-Pfr transition (Takala et al., 2014); and (3) the long helix along the dimer interface, which spans along the entire PAS/GAF and PHY domains (Essen et al., 2008; Yang et al., 2008, 2015) (Figures 1A and 1B). The C-terminal effector domain is divergent between species and is often a histidine kinase in BphPs (Auldridge and Forest, 2011; Gourinchas et al., 2017; Otero et al., 2016; Woitowich et al., 2018; Yang et al., 2015). Full-length phytochromes are difficult to crystallize, but the PCM of some BphPs forms crystals that diffract to 2-Å resolution and beyond (Sanchez et al., 2019). They are particularly suited for time-resolved crystallographic investigations.

Phytochromes display a photocycle (Figure 2A) with two half cycles that are driven by two different wavelengths of light. In most phytochromes, the dark-adapted state, denoted as Pr, absorbs red light ($\lambda \sim 700$ nm), which causes a *Z*-to-*E* isomerization of the C15=C16 double bond within its bilin chromophore (Figure 2B). Subsequent conformational changes of the entire protein end in a far-red-light-absorbing state, denoted as Pfr. The Pfr state either relaxes thermally back to Pr or can be driven back to Pr by far-red light ($\lambda \sim 750$ nm). The structural changes associated with the Pr-to-Pfr transition modulate the enzymatic activity of the phytochrome (Giraud et al., 2005; Gourinchas et al., 2018). Although the Pr and Pfr states have been structurally characterized in detail using the *Deinococcus radiodurans* (*Dr*) BphP PCM (Burgie et al., 2016; Essen et al., 2008; Takala et al., 2014; Yang et al., 2008), structures of the nanosecond intermediates Lumi-R and Lumi-F as well as those of the longer-lived intermediates in each photo-half-cycle (Figure 2A) are missing. In the Lumi-R intermediate, the BV chromophore is in the electronic ground state. The 15*Z* anti-isomerization (Figure 2B) to 15*E* anti-isomerization of the C15=C16 double bond between rings C and D of the BV chromophore should have taken place, which results in a significant rotation of the D ring (Mathes et al., 2014; Schmidt et al., 2007; Toh et al., 2010) (Figure 2A).

Through the latest developments in time-resolved serial X-ray crystallography (TR-SFX), the 1-ps structure of the truncated *Dr*BphP chromophore-binding domain (CBD) that consists only of the PAS and GAF domains was determined (Claesson et al., 2020). One picosecond after photoexcitation, the BV D ring in the *Dr*BphP CBD rotates counterclockwise while the PW is photoejected from the chromophore-binding pocket. Displacements of important, conserved amino acid residues are already observed at 1 ps. For example, the conserved Asp207 in the GAF domain moves significantly, which implies signaling directed toward the PHY sensory tongue. However, the PHY domain is not present in the CBD construct. Experiments on the entire PCM including the critical PHY domain and sensory tongue are necessary to understand how the light signal is transduced to the C-terminal enzymatic domain.

Previous attempts to initiate the photocycle in PCM crystals of various BphPs at room temperature were unsuccessful presumably because the PCM constructs were not photoactive in the crystal form, the illumination protocol was suboptimal, and/or the spatial resolution reached at room temperature was not sufficient (Roessler et al., 2016; Woitowich et al., 2018). Recently, we published the structure of a class I BphP from non-photosynthetic myxobacterium *Stigmatella aurantiaca*, denoted *Sa*BphP2 PCM. The structure was solved to a resolution of 1.65 Å at cryogenic temperatures (100 K) in the Pr form (Figure 1B). *Sa*BphP2 PCM crystals are weakly photoactive, as demonstrated by the static spectra in Figure 2C. Microcrystals diffract to 2.1-Å

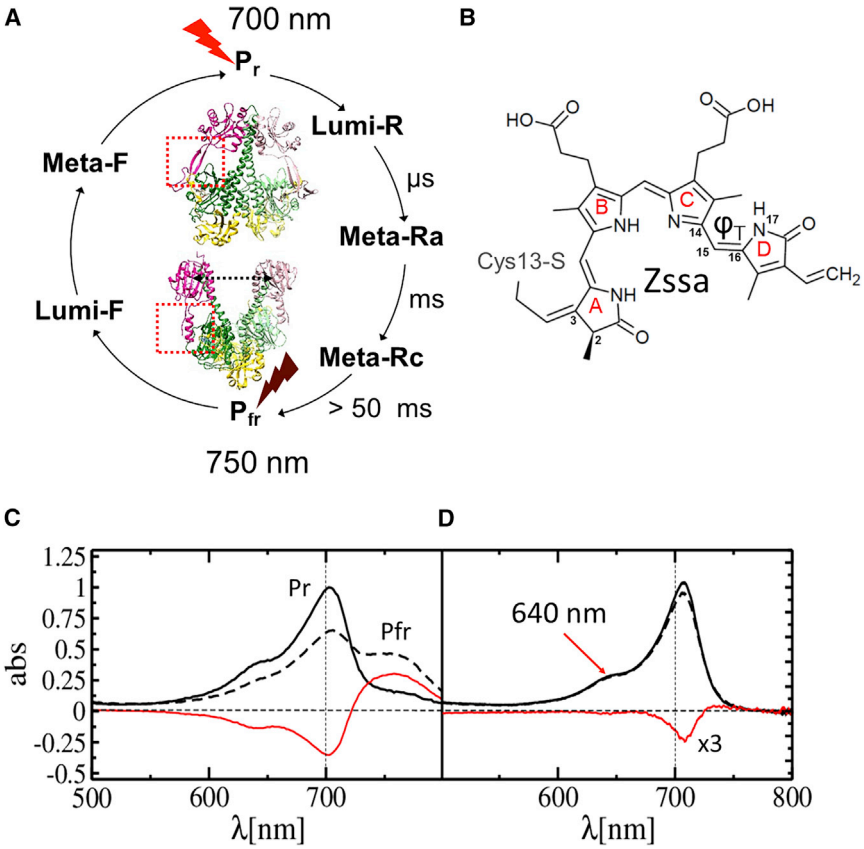

Figure 2. Phytochrome photocycle and UV-visible absorption spectra of *Sa*BphP2

(A) Phytochrome photocycle. Approximate time scales for intermediate (Lumi-R, Meta-Ra, and Meta-Rc) formation are shown. Pfr is formed after about 50 ms with variations between different BphPs. The two half cycles can be driven by illuminating the stable Pr and Pfr states (displayed for the *Sa*BphP2 and *Dr*BphP PCMs, respectively) by red and far-red light.

(B) The chemical structure of BV bound to Cys13 in the phytochrome. The torsional angle ϕ_T that defines isomerization/rotation about the double bond Δ15,16 is indicated. In Pr the structure is all-*Z* syn-syn-anti.

(C) Static absorption spectra of the *Sa*BphP2 Pr (solid line) to Pfr (dashed line) transition in solution. The difference is shown in red.

(D) As (C) but in the crystal. The transition is initiated by 640 nm LED light (arrow). The difference (red line) is enhanced 3-fold.

resolution at room temperature (Sanchez et al., 2019), which provides an opportunity to describe the Pr-to-Pfr transition by TR-SFX experiments.

The TR-SFX experiments on the *Sa*BphP2 PCM reported here were conducted at the Japanese X-ray free electron laser (XFEL), the Spring-8 Angstrom Compact X-ray Laser (SACLA) (Figure 3A). They resulted in room-temperature structures 5 ns and 33 ms after light illumination of the Pr (dark) state with 640-nm laser pulses (Figures 3C and 3D; Table 1). To be able to analyze the signal that is expected from the small spectral response (Figure 2D), high-quality data are required. More than 30,000 indexed diffraction patterns were collected per time delay that resulted in datasets to 2.1-Å resolution with R_{split} values smaller than 10% (Table 1). Results are discussed in terms of extensive rearrangements of BV, specifically the D ring, the PW with the neighboring water network, and conserved amino acids in the GAF and PHY domains.

RESULTS

Difference electron density at 5 ns and 33 ms

The difference electron density (DED) maps calculated at the 5-ns and 33-ms time delays show a large number of correlated positive and negative DED features in the PAS-GAF as well as in the PHY domains (Figure 4 and Table S1). These features indicate structural changes through the entire *Sa*BphP2 PCM dimer. The control map at 67 ms only contains spurious features (Figure 4A, 66 ms), which shows that a once excited jet volume entirely left the X-ray interaction region. In all previous nanosecond time-resolved crystallographic experiments on photoactive yellow protein (Jung et al., 2013; Tenboer et al., 2014), myoglobin (Schmidt et al., 2005; Srajer et al., 1996), and others (Nogly et al., 2018; Skopintsev et al., 2020), DED features are mostly localized to the chromophore and a few residues. As a consequence, the DED map sigma level is determined by the noise in the DED map as has been shown previously (Srajer et al., 2001). Here, the map sigma level is determined by both the noise and the signal (Figure 4B). More than 1,000 DED features larger or smaller than ±4σ, respectively, that were found in the unit cell (Table 2) pose a formidable challenge for the interpretation of the DED maps as well as for structure determination. The features must be interpreted locally near the chromophore and the chromophore pocket, and more globally for the entire *Sa*BphP2 PCM dimer. Standard deviations (σ) of the DED maps at 5 ns and 33 ms are determined by both the noise and the signal (Figure 4B). We therefore contour the DED maps using multiples (typically a factor of 3) of the σ values of the 67-ms control DED map to identify chemically meaningful DED features (Figure 5).

D-ring orientations at 5 ns and 33 ms

Substantial DED features are observed on and near the BV chromophore (Figures 4A and 5). Strong negative DED features on the D-ring carbonyl, methyl and vinyl mark substantial structural rearrangements in both subunits. Interestingly, positive features that identify D-ring orientations upon light illumination differ in subunit A and subunit B. In subunit A, there are strong lateral features (β_1 to β_4) that support a clockwise ~90° twist of the D ring when viewed along the chromophore axis from the D ring to the A ring (Figures S1B and S1D). These features can be reproduced by calculated difference maps (compare Figure S1C and S1E). In addition, positive features ξ (Figure 5A) are oriented in a way that supports a ~180° rotation. For the

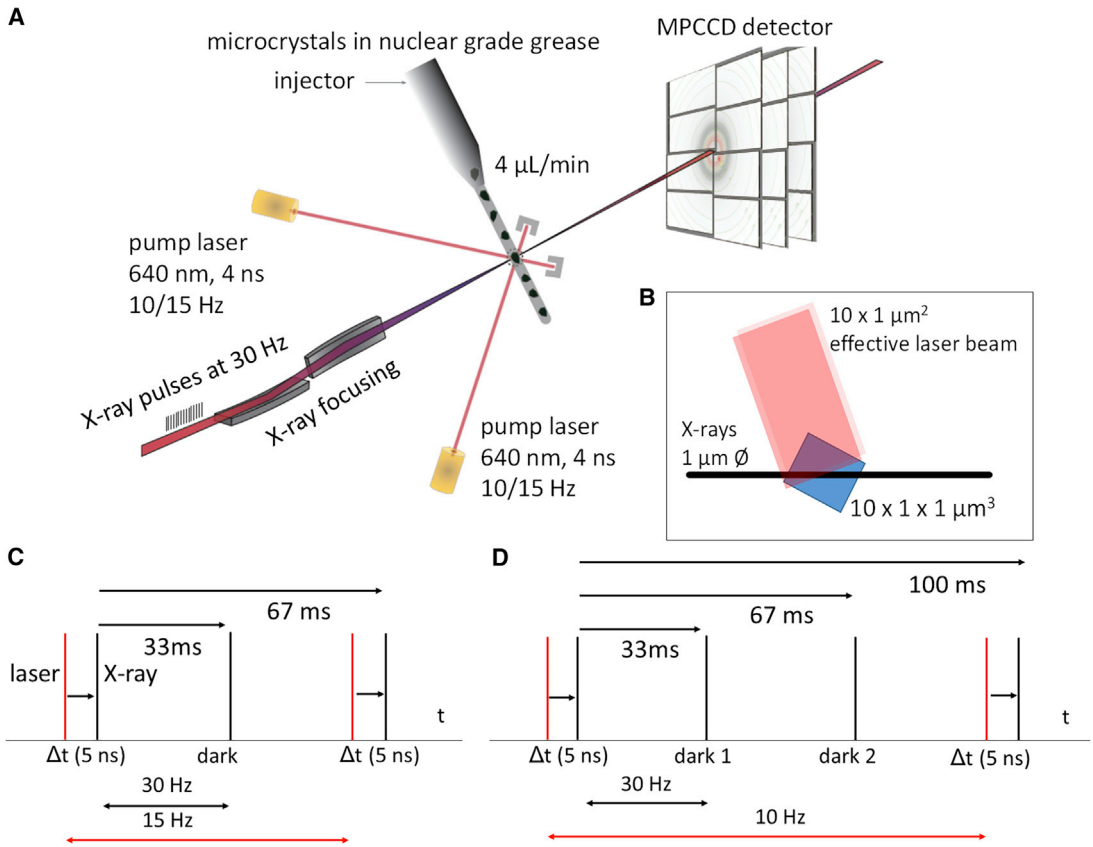

Figure 3. Data collection at SACLA

(A) Crystals embedded in nuclear grease are injected into the X-ray interaction volume. Before they are probed by X-rays, they are excited from two sides by nanosecond laser pulses.

(B) Effective laser beam geometry to excite the entire volume probed by the X-rays in the quasi-perpendicular geometry shown in (A).

(C) Pump-probe data collection with one dark exposure (dark, 33 ms) in between the laser pulses.

(D) Pump-probe data collection with two dark exposures (dark 1, 33 ms and dark 2, 67 ms) in between the laser pulses. This scheme was used to assess whether a laser-excited jet volume left the X-ray interaction region after 67 ms.

interpretation of features ξ, extrapolated electron density (EED) maps were necessary, since the strong negative density on the D-ring carbonyl tends to eliminate nearby positive features. Ring-like electron density appears in the EED maps (Figure 5B), indicating a fully isomerized D ring. Accordingly, two conformations of the chromophore are needed to interpret the positive DED to completion, a ~90° clockwise D-ring twist, and a fully isomerized ~180° clockwise D-ring rotation (Figure 5B and Table 1). D-ring rotations were assessed by (1) measuring the change ($\Delta\varphi_T$) of the torsional angle φ_T defined by atoms C14-C15=C16-N17 (see Figure 2B), and (2) by determining the angular change $\Delta\varphi^{\perp}$ of the normal vector $V^{\perp}$ on the D-ring plane between the reference structure in the dark and at each time delay. The results are shown in Table 3.

In subunit B, features ξ are absent (Figure 5C). In accordance, EED maps (Figure 4D) do not support a fully isomerized configuration. The clockwise ~180° rotation as in subunit A is not observed for both the 5-ns and the 33-ms time delays. Nevertheless, strong positive features determine the geometry of the BV A to C rings; see Figures 5A and 5C for a comparison of the DED in both subunits. In subunit B the entire BV pivots about the B ring (Figure 5C), which leads to strong C-ring and D-ring displacements. To interpret positive features β_{c1} and β_{c2} ("c" for clockwise), the C ring must be tilted backward (blue arrow in Figure 5C), and the D ring can only be oriented clockwise (light-blue BV structure in Figures 5C and 5D) to fit the DED. This leaves a strong feature β_{a1} ("a" for anti-clockwise), which is located behind the C-ring propionyl group. To reproduce this feature, the C-ring propionyl group must tilt in the opposite direction (purple arrow in Figure 5C), which leads to a displacement of carbon atom C_{15} forward (feature β_{a2}). The counterclockwise D-ring orientation (in pink) then fits the DED.

In summary, we observe a ~90° clockwise D-ring twist and a fully isomerized ~180° clockwise D-ring rotation in subunit A. In subunit B we observe a clockwise and a counterclockwise D-ring twist. In addition, both conformations are associated with significant C-ring tilts (Table 3). In all structures the A and B rings have retracted from their positions and the propionyl groups undergo rearrangements so that they change their connection points in the chromophore-binding pocket (see Figures 5A and 5C).

Table 1. Data collection statistics

	Dark	5 ns	33 ms	66 ms
Beamline	SACLA BL2			
Resolution (Å)	2.1			2.3
Temperature (K)	285			
Space group	$P2_1$			
Unit cell parameters	a = 83.7 Å, b = 83.4 Å, c = 86.9 Å; α = 90°, β = 107.6°, γ = 90°			
Observations	35,170,843	30,128, 819	30,917, 561	10,193, 417
No. of unique reflections	68,911	68,919	68,919	53,717
Redundancy	510 (111)	437 (135)	449 (154)	190 (124)
Completeness (%)	100.0	100.0	100	100
$CC_{1/2}$ at d_{min}	0.11	0.16	0.21	0.31
R_{split} (%)	11.1 (221.9)	9.4 (109.4)	9.4 (101.6)	18.1 (157.2)
Max/min $\Delta\rho$ (σ)	reference	7.0/−8.6	6.7/−8.6	5.2/−4.9
R_{cryst}/R_{free} (%)	19.5/23.7	31.4/34.1	29.3/33.3	–
RMSD to reference (Å)[a]	NA	1.4	1.5	–

[a]Root-mean-square deviation of C_α atoms in structures at time delays 5 ns or 33 ms relative to corresponding C_α atoms located in the dark-state structure. NA, not applicable.

Amino acid and water network rearrangement in the chromophore-binding pocket and the sensory tongue

Strong negative DED features indicate that the PW has been photoejected from BV in both subunits at 5 ns and 33 ms (Figure 5 and Table S1). Moreover, significant displacements of the conserved Asp192 of the PASDIP motif in the GAF domain and the Arg457 of the PRXSF motif (Essen et al., 2008; Toh et al., 2011b) in the PHY domain are observed in subunit A (and at 33 ms also in subunit B). Asp192 and Arg457 form a salt bridge, anchoring the PHY tongue to the chromophore region in the Pr state. This connection is broken at 5 ns. A strong positive DED feature between these two amino acids is observed, indicating a water molecule (Figure 5A). Furthermore, the conserved Tyr248 in proximity to Asp192 adopts a dual conformation at 5 ns and 33 ms (Figures S2D–S2F). Similarly, a dual conformation is observed for the conserved His275 (at 33 ms) that forms a hydrogen bond to the D-ring carbonyl in the Pr state of the *Sa*BphP2 and other classical BphPs. In contrast to these amino acid rearrangements, the structure of the sensory tongue is only locally affected (Figure 6C). A β-sheet to α-helix transition is not observed, which coincides with only minor changes of the PHY domain position (Figures 6D and 6E).

On the other side of the chromophore, opposite to the tongue region, strong features in the DED maps at 5 ns and 33 ms indicate that the BV C-ring propionyl group drags the conserved Ser257 and Ser259 along at 5 ns and 33 ms (Figure 6B; see also Tables 2 and 3). A positive DED feature in the B subunit indicates the appearance of a water molecule that may form hydrogen bonds with the C-ring propionyl as well as with Ser257 and Ser259. Moreover, the DED maps show correlated negative and positive features within the PAS-GAF domains and along the long helices that form the dimer interface (Figure 4A), pushing outward the C-terminal helix that connects to the output module (Figures 6D and 6E). We propose that the structural changes in the chromophore pocket initiate the signal that is transduced along the long helices "wiring" together the BV chromophore and effector domains.

DISCUSSION

Global and local structural relaxations at 5 ns and 33 ms after illumination

On the nanosecond timescale the signal is expanding through the entire *Sa*BphP2 PCM (Figure 3A), and structural changes in the chromophore, the surrounding amino acids, and in distant parts several nanometers from the chromophore are observed. The displacements of the chromophore and in the surrounding residues are much larger than in the related CBD fragment (which lacks the PHY domain) of *Dr*BphP at 1 ps and 10 ps (Figure 3A) (Claesson et al., 2020). *Sa*BphP2 is large and flexible and can react readily and quickly to the local, light-induced chromophore conformational changes. In the CBD of *Dr*BphP, the chromophore essentially stays at the position that it also occupies in the dark structure (Claesson et al., 2020). Despite the small chromophore displacement at 1 ps, the signal has already penetrated deep into the BV-pocket of the GAF domain. From the present structures of SaBphP2 PCM on the nanosecond and microsecond timescales, we find that these relaxations evolve, become more extensive, and affect almost the entire PCM structure (Figure 4A).

Especially in subunit B, large chromophore geometry distortions of the BV chromophore are present (Table 1) as the C ring tilts out in both directions (Figure 5C). Not only the D ring but also the C ring is affected by the isomerization. Despite the fact that the torsional angle φ_T changes by more than 100° for subunit B, the actual D-ring rotation $\Delta\varphi^{\perp}$ (measured by the D-ring normal vector $V^{\perp}$) is smaller, in the range of 80° (Table 3). The difference between $\Delta\varphi_T$ and $\Delta\varphi^{\perp}$ is absorbed by the C-ring tilt. This can be also observed for the BV in subunit A to a lesser extent, except that the D-ring normal vector reorients by about 170° and 70° for the fully isomerized form and the partial clockwise twist, respectively. These structures capture how part of the energy of the absorbed photon is stored in a distorted BV geometry that drives protein relaxations.

Chromophore geometry distortions are also found in early intermediates of unrelated proteins such as the PYP (Jung et al., 2013). Distortions of the BV chromophore in the phytochrome photocycle have been predicted by time-resolved spectroscopy (Toh et al., 2010). They were directly observed in temperature scan cryo-crystallography experiments performed on the bathy phytochrome *Pa*BphP from *Pseudomonas aeruginosa* (Yang et al., 2011) (Table S2), further suggesting that distorted chromophore conformations are part of an important mechanism to advance photochemical reactions. As the BV chromophore position changes, it strongly affects amino acid residues near the BV propionyl moieties that shift in unison with the chromophore

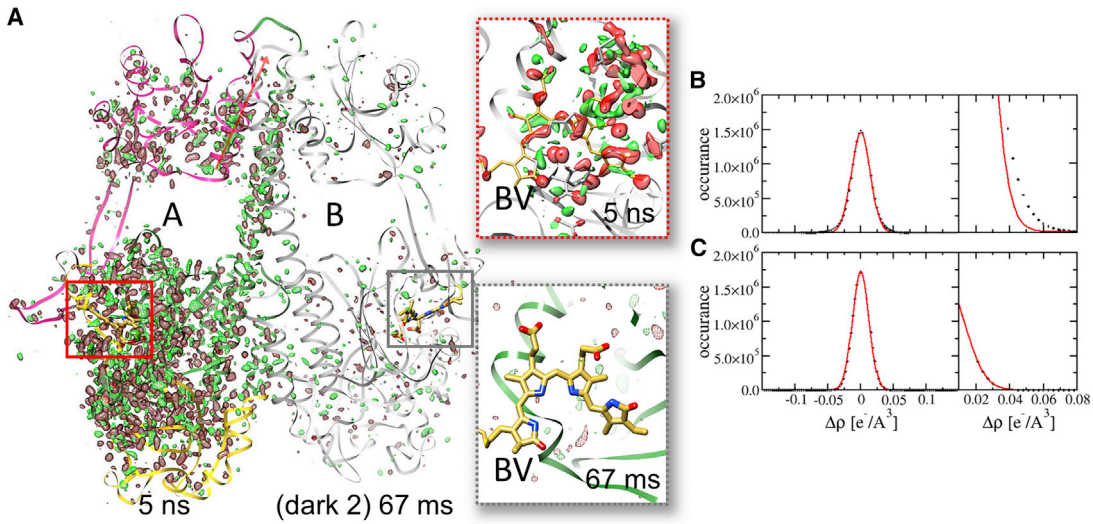

Figure 4. Difference maps for 5-ns and 66-ms time delays overlaid on the *Sa*BphP2 PCM dimer

(A) The 5-ns DED map is displayed with subunit A and the 66-ms DED map with subunit B (gray). Contour levels: red −3σ, green 3σ. PAS, GAF, and PHY domains of subunit A are shown in yellow, green, and magenta, respectively. Red arrow shows direction of the C-terminal helix that connects to the coiled-coil linker in the full-length BphP. Note the numerous DED features along the dimer-interface helix into the PHY domain and the C-terminal helices at 5 ns. Insets show the corresponding difference maps in the biliverdin (BV) binding pocket. At 66 ms, only spurious, random DED features are present. The chromophore is essentially free of signal.

(B) Histogram of DED features in the DED map at the 5-ns delay with extensive signal. The Gaussian (red line) does not fit the flanks.

(C) Histogram of DED features in a DED map without signal. The Gaussian fits the flanks properly.

displacements. Examples of amino acid displacements in the *Sa*BphP2 PCM and other phytochromes are listed in Tables 3 and S2, respectively, and are discussed later. The species with the nearly 180° D-ring rotation might be associated with a key Lumi-R-like intermediate in the phytochrome photocycle (Figure 1A). To determine the specific time point when the 180° rotation begins, additional data collected at different time delays are required.

Table 2. Observed DED features and expected random DED features at the 33-ms time delay

Feature (sigma)	Observed	erf (*x*/2)	PI 1 − erf (*x*/2)	erf $(x/2)^N$	PM 1 − erf $(x/2)^N$	Expected random features in the DED map $N \times (1 - \mathrm{erf}(x/2))$
1	>8,000	0.68	0.31	0.0	1.0	216238
2	>8,000	0.95	0.05	0.0	1.0	31,007
3	3,167	0.997	0.002	0.0	1.0	1,839
4	1,018	1.0	0.0	0.0	1.0	43
5	264	1.0	0.0	0.67	0.33	0.4
6	44	1.0	0.0	1.0	0.0	0.0

Random features were estimated as a function of a multiple (*x*) of sigma (sigma level) in the unit cell of the *Sa*BphP2 difference map calculated on an 88 × 88 × 88 grid (N = 681,472). The number of observed peaks was determined by the ccp4 program peakmax as a function of the DED sigma value. PM is the probability of observing at least one random feature equal to or more than a given sigma level in the entire map, as opposed to the probability PI of observing this random feature in an individual voxel. Note that we write (1 − erf) rather than using the equivalent erfc, where erf is the error function.

The absence of the fully isomerized D-ring isoform in subunit B can likely be explained by differences in the subunits related by non-crystallographic symmetry. As the structure of the sensory tongue is essentially identical in both subunits, it is unlikely to be the reason for this behavior. By inspecting the region near Cys13 to which the BV chromophore is bound, differences are found between the A and B subunits. Specifically, distances to symmetry-related molecules are different for subunits A and B. In subunit A the distances from Arg15 to Gln139 and Cys13 (S) to Lys136 (N_z) (Gln139 and Lys136 belong to the molecule related by crystallographic symmetry) are 6.0 Å and 7.2 Å, respectively. These distances are smaller in subunit B (5.2 Å and 4.0 Å, respectively). These differences likely have an impact on chromophore relaxations, as in subunit B the BV structure appears more distorted than in subunit A (see twisting angles for subunits A and B in Table 1).

Rearrangement of water network and neighboring amino acids

The PW forms a stable hydrogen bond network with BV rings A–C in both the Pr and Pfr states, but it is absent at 5 ns and 33 ms (Table S1). This light-induced ejection of the PW already occurs within 1 ps in the *Dr*BphP CBD fragment (Claesson et al., 2020). While the twisting motion of D ring has been the working model for phytochrome activation and now has been confirmed, the disappearance of the PW is nevertheless surprising. Given the large sliding motions of the chromophore (Figures 4A and 4C), this now makes sense as the absence of the PW

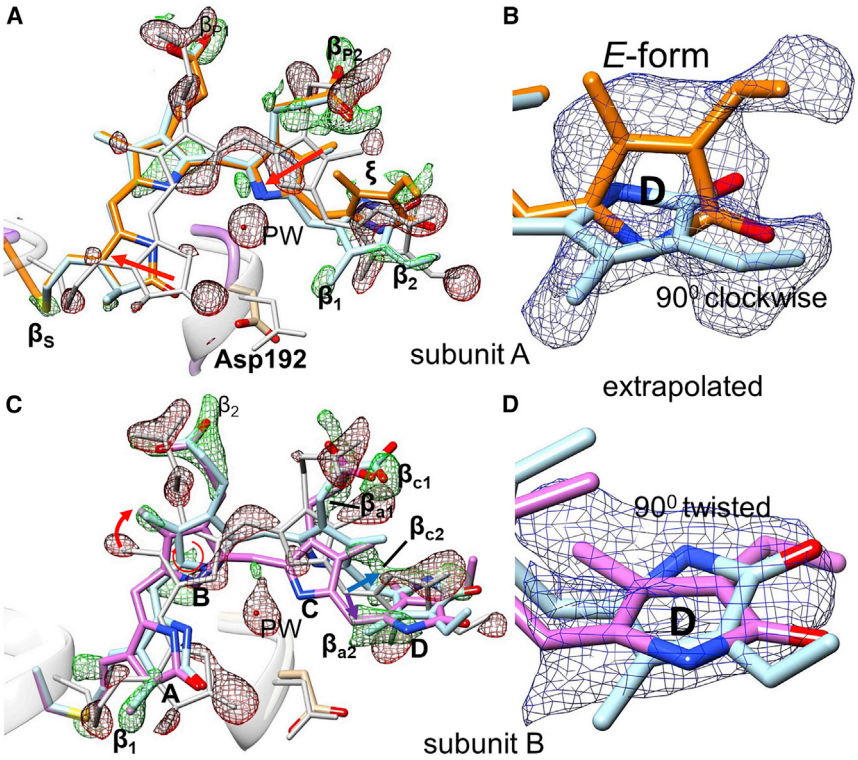

Figure 5. Chromophore displacements and D-ring rotations

DED is displayed in red and green with contour levels red, -2.7σ (-3σ of DED_{66ms}); green, 2.7σ (3σ of DED_{66ms}). EED is shown in blue with $N_c = 22$ (B) and $N_c = 19$ (D), contour level 1.5σ.

(A) Overall chromophore configuration in subunit A at the 33-ms time delay. Gray, reference (dark); orange, intermediate at 33 ms. For subunit A the reference structure is gray, the result of the clockwise D-ring rotation light blue, and the fully isomerized structure orange. Chromophore slides in the direction of the red arrows. PW, pyrrole water.

(B) EED (blue), $N_c = 22$, on the D ring in subunit A, colors as in (A).

(C) Chromophore configuration in subunit B at 5 ns. Positive features β determine the ring positions. Feature β_{c2} (behind the chromophore plane) is the result of a C-ring tilt resulting in a clockwise rotation of ring D (light-blue structure and blue arrow). Feature β_{c2} denotes a C-ring tilt forward, which results in a counterclockwise rotation of ring D (pink structure and purple arrow).

(D) EED (blue) on the D ring in subunit B, colors as in (C).

most likely enables these displacements. It is interesting to note that the PW is ejected very early (Claesson et al., 2020) and rebinds back to BV in Pfr (Burgie et al., 2016; Takala et al., 2014). The PW may have a dual role in facilitating the structural transition and stabilizing the reaction product (Pr as well as Pfr) in both halves of the reaction cycle. Both the rotation of the D ring and photoejection of the PW likely are the main triggers for subsequent protein structural changes. Together, they transduce the light signal to the sensory tongue of the PHY domain and cause relaxations of the GAF domain that propagate further up the long helices along the dimer interface.

Sensory tongue and the PHY domain

The sensory tongue connects the PHY domain directly with the chromophore region (Figure 6). During the full Pr-to-Pfr transition the sensory tongue undergoes extensive structural transitions from a β sheet to an α helix (Burgie et al., 2016; Takala et al., 2014). In the Pfr state, Pro456 of the PRXSF motif in the PHY domain locates adjacent to the D ring and forms a hydrogen bond with Tyr248, thus stabilizing the D ring in E configuration. An interesting question is how this shift is initiated. In our TR-SFX experiments, this transition is not observed (Figure 6C). We ascribe this to the crowded environment of the crystals. However, the tight Asp192-to-Arg457 salt bridge is already broken at 5 ns and a water is inserted between the residues. This is an important first step to enable the sensory tongue to rearrange. We therefore conclude that the signal is transduced to the PHY tongue via the displacement of the chromophore that enforces the movement of Asp192 and the photoejection of the PW.

Propagation of the light signal

Owing to D-ring rotation, the conserved Tyr248 moves (Figures S2D–S2F). This destabilizes interactions with the neighboring amino acids and the water network. Arg457 and Asp192 form new hydrogen bonds with a water molecule (Figure 6A). As the chromophore slides substantially (Figure 5), it induces structural changes in the GAF domain sensed by the conserved serines 257, 259, and 261 and multiple other amino acids near the chromophore. His275 loses contact with the D- ring carbonyl (distance: >4 Å) and with the more distant Arg157 (now ~4.0 Å) that lead to substantial GAF domain relaxations which are ultimately relayed to the PHY domain through the long dimer-interface helices. As the speed of sound in protein crystals is about 2,000 m/s (Speziale et al., 2003), heat expansion through 100 Å of protein (roughly the length of the *Sa*BphP2 PCM) in 5 ns cannot be excluded. However, relaxations at 33 ms are very similar to those at 5 ns. Heat produced locally after chromophore light absorption should have dissipated by then, and the DED features at 5 ns rather represent genuine protein relaxations.

The changes on the long dimer helix and the C-terminal helix (Figure 3) suggest a mechanism of signal transduction that does not rely exclusively on the refolding of the PHY tongue and the associated movement of the PHY domains (Figure 2A). Instead, the long helices translate the signal toward the small C-terminal helices that are connected to the coiled-coil linker region of the effector domain (Figures 1A, 6D, and 6E, red arrows). This confirms a suggestion that was based on the static crystal structures of the bathy *Pa*BphP PCM (Yang et al., 2008) and more recently on solution nuclear magnetic resonance (NMR) (Gustavsson et al., 2020; Isaksson et al., 2020). This compares favorably with the general

Table 3. Comparison of the reference (dark) and the 5-ns and the 33-ms *Sa*BphP2 PCM structures

	Reference (Pr)		5 ns[a]		33 ms[a]	
	A	B	A	B	A	B
Asp192-O/A-ring N	3.0	3.3	3.1/3.1	4.4/4.0	**3.8/4.0**	**4.1/4.6**
Asp192-O/A-ring carbonyl	4.5	4.4	4.1/4.1	5.5/5.8	4.5/5.1	5.4/5.6
Asp192-OD2/A-ring carbonyl	3.2	3.2	**4.1/4.1**	**4.1/4.1**	3.4/**4.6**	**3.9/4.1**
Asp192-O/B-ring N	3.0	3.0	2.9/3.0	3.1/3.3	**4.2/4.3**	**3.3/3.3**
Asp192-O/C-ring N	2.9	3.0	**3.8/4.1**	**5.1/5.2**	**5.1/5.1**	**4.7/5.0**
Asp192-OD2/Arg457-NH	2.6	2.9	**5.4**	3.0	**4.4**	**4.8**
Asp192-OD2/Tyr161-OH	5.6	5.7	5.5	4.9	5.6	4.2
Asp192-OD2/Tyr248-OH	2.7	2.7	**3.5/3.5**	**5.8/5.3**	**5.3/5.5**	**3.9/4.4**
Tyr248-OH/D-ring methyl	3.5	3.5	2.7/4.2	3.4/>5.0	2.6/3.9	2.9/5.3
Tyr248-OH/Arg457-NH1	4.2	4.4	3.5/**>5.0**	3.5/4.3	5.3/5.5	4.8/5.5
Ser242-N/B-ring propionyl O2	2.9	2.8	**5.1/5.1**	**4.3/>5.0**	**3.3/3.3**	**5.2/5.7**
Ser257-OG/C-ring propionyl O2	3.2	2.5	2.3/2.6	2.6/**3.9**	2.6/**3.3**	**3.5/5.0**
Ser259-OG/C-ring propionyl O2	2.7	2.7	3.1/3.3	2.6/2.5	2.1/**3.5**	2.3/2.4
Ser259-OG/Arg207-NH2	2.9	2.8	**5.1**	**4.7**	**4.4**	**5.4**
His275-NE2/C-ring propionyl O2	4.7	6.2	6.0	7.1/7.2	6.7/6.9	6.2/7.5
His275-NE2/D-ring carbonyl	3.0	2.8	**6.0**	2.8/**4.3**	**4.3/4.8**	3.3/**4.4**
His275-ND1/Arg157-NH2	2.9	2.9	**3.6**	**3.8**	2.7/**4.8**	**4.5**
His245-ND1/B-ring N	3.5	3.6	3.6/3.8	3.7/3.8	3.7/3.7	5.1/5.3
His245-ND1/C-ring N	3.4	3.6	3.7/3.8	4.2/4.7	3.7/3.8	4.6/5.4
His245-NE2/C-ring propionyl O1	2.6	2.8	2.7	2.9/**3.8**	3.0/**3.5**	**3.4/5.4**
Arg457-NH1/A-ring carbonyl	4.5	4.5	6.0	5.4/5.5	7.4/7.4	7.0/7.2
Tyr201-OH/Arg207-NH1	4.0	3.9	3.7	4.0	4.9	**3.0**
Tyr201-OH/B-ring propionyl O1	2.7	2.8	2.9	2.7/3.1	2.8/2.9	2.3/3.1
Tyr201-OH/C-ring propionyl O1	5.9	5.9	4.4/5.9	5.0/5.0	5.9/6.1	5.7/5.7
Ser261-OG/Arg207-NE	3.1	2.7	**3.6**	**4.0**	**3.6**	**4.0**
Arg207-NH2/C-ring propionyl O1	5.4	5.3	4.9/6.1	4.1/5.7	4.1/5.1	3.9/4.2
Arg239-NH2/B-ring propionyl O1	2.7	2.9	2.4	2.5/2.6	**3.8/3.9**	2.8/2.9
A-ring torsion (°)	7	9	12/20	40/40	7/-1	15/39
D-ring torsion, φ_T (°)	32	27	−61/−151	134/−88	−62/−160	132/−100
B/C-ring relative tilt (°)	11	14	25/25	43/37	32/46	43/46
$\Delta\varphi_T$, D-ring torsion (°)[b]	–	–	−93/ **−183**	102/ −120	−94/ **−192**	105/ −127
$\Delta\varphi^{\perp}$, D-ring normal vector (°)[c]			72/**172**	73/92	59/**171**	87/74

Bold entries: important interactions; bold numbers: large changes relative to the reference structure.
[a]Separately for alternative conformations, if present.
[b]Difference between D-ring torsion φ_T in the dark and at measured time delays. Negative values: clockwise rotation relative to dark, positive values: counterclockwise rotation relative to dark, bold red: *E* configuration.
[c]Angular difference between the D-ring normals measured in the dark and at various time delays.

notion that signal transduction in transmembrane sensory proteins is conducted through the long helices (Gushchin et al., 2017). Only small PHY domain displacements (Figures 6D and 6E) are necessary for signal transduction. Since the linker helices of the sister monomers are at an angle, translations along their axes will slightly change the relative orientation of the effector domains and, hence, their activity, possibly modulated by a shift in register of the coiled-coil linker (Gourinchas et al., 2018).

CONCLUSIONS AND OUTLOOK

The short-lived structural intermediates presented here establish that it is indeed the isomerization of the D ring that drives the photoconversion in phytochromes. However, the remaining rings of the chromophore move notable distances, and the movements are heterogeneous between the different subunits. We consider some of the BV conformations to be unproductive, which may explain the relatively low quantum yield for the Pr-to-Pfr transition (approximately 10%–15%). Nevertheless, we observe a fully isomerized BV configuration and establish that the photoejection of the PW and the displacements of the strictly conserved Asp195 and Tyr248 lead to a disconnection of the PHY sensory tongue from the chromophore region. Finally, the data show strong evidence for a structural change along the long helices at the dimer interfaces that transduce the signal further toward the PHY domains.

Earlier time points within the *Sa*BphP2-WT PCM photocycle should be collected to assess when the large BV chromophore

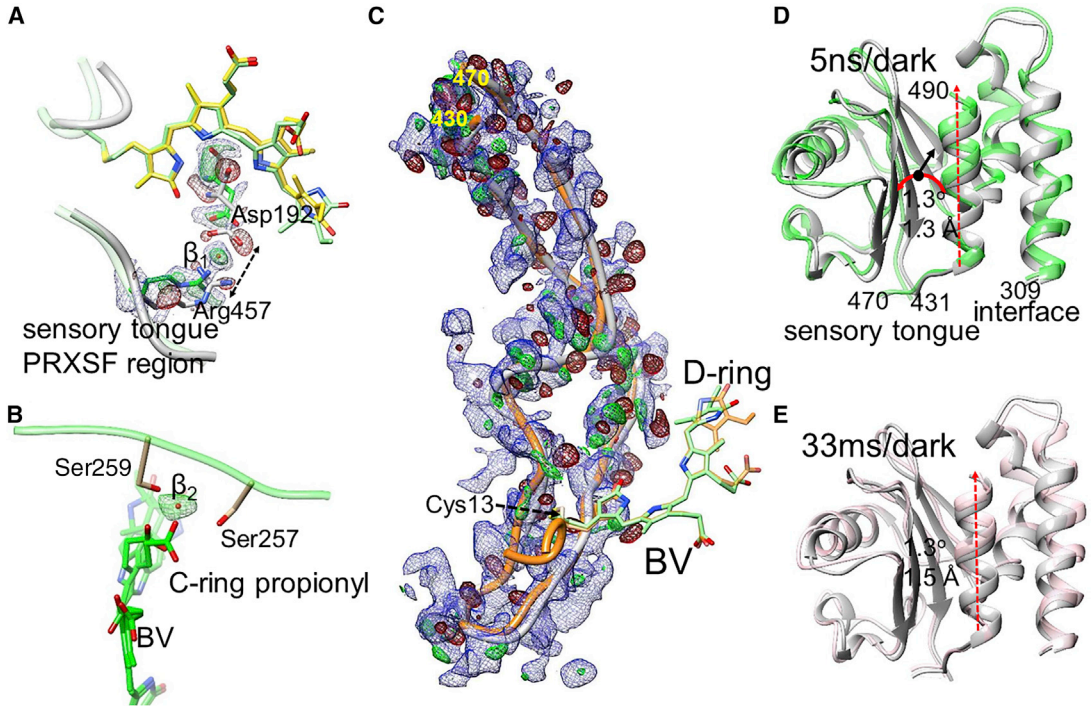

Figure 6. Local and global structural changes

DED in red and green (±3σ contour), EED in blue (1.2σ contour).

(A) Separation of the sensory tongue from the BV binding region (dotted arrow) in subunit A (5 ns). Asp192 and Arg457 are indicated. The BV chromophore with the 90° twisted and fully isomerized D ring is shown in yellow and green, respectively. The positive DED feature β_1 is interpreted by a water molecule.

(B) The BV (green) C-ring propionyl group detaches from Ser257 and Ser259, which coordinate a water (feature β_2, green positive DED) instead. The structure is displayed for subunits B (33 ms) where the D ring twists ~90° both clockwise and counterclockwise.

(C) The sensory tongue region. Gray, structure of the reference state; orange, structure at 33 ms. Residues at the beginning and the end of the region are indicated. The chromophore is shown with the twisted D ring (green) and the fully isomerized form (orange).

(D) The PHY domain region. Comparison of the 5-ns structure (green) with the reference structure (gray). Sequence numbers are indicated. The PHY domain centroid (black dot) moves by 1.3 Å (black arrow) and rotates (red curved arrow) by 1.3°. The connection to and from the sensory tongue is marked.

(E) The PHY domain at 33 ms versus reference. Displacements similar to those in (A) are observed. In (D) and (E), the displacement of the C-terminal helix is marked by the red dashed arrow.

displacements begin. Large-scale structural changes are limited by the crystal packing. Therefore, methods that act on proteins in solution should be explored to make further progress. Recently, solution NMR spectra of a full PCM were assigned for a phytochrome (Gustavsson et al., 2020), and new developments in cryoelectron microscopy (Nogales, 2016) bring near-atomic resolution of macromolecular structures within reach without the need for crystals. Calculations are under way (Poudyal et al., 2020) to explain how to obtain structures from single biological macromolecules, such as the full-length, intact BphPs at XFELs.

STAR★METHODS

Detailed methods are provided in the online version of this paper and include the following:

- KEY RESOURCES TABLE
- RESOURCE AVAILABLITY
  - Lead contact
  - Materials availability
  - Data and code availability
- EXPERIMENTAL MODEL AND SUBJECT DETAILS
- METHOD DETAILS
  - Protein purification and crystallization
  - Experimental design
  - TR-SFX data acquisition and processing
  - Computation of difference electron density maps
  - Structure determination
  - Pearson correlation for Ring-D orientation
  - Detailed views of structural moieties
- QUANTIFICATION AND STATISTICAL ANALYSIS
  - Statistical analysis of DED features

SUPPLEMENTAL INFORMATION

Supplemental information can be found online at https://doi.org/10.1016/j.str.2021.03.004.

ACKNOWLEDGMENTS

This work was supported by National Science Foundation (NSF) Science and Technology Centers (STC) grant NSF-1231306 ("Biology with X-ray Lasers"). Some results shown are derived from work performed at Argonne National Laboratory, Sector 14 - BioCARS at the Advanced Photon Source. Argonne is operated by UChicago Argonne for the US Department of Energy, Office

of Biological and Environmental Research under contract DE-AC02-06CH11 357. The experiments at SACLA were performed at BL2 with the approval of the Japan Synchrotron Radiation Research Institute (proposal nos. 2018A8055 and 2019A8007). E.A.S. was supported by NSF-MCB-RUI 1413360, NSF-MCB-EAGER grant 1839513, and NSF STC BioXFEL center award 6227. Training of M.N. and L.A. was supported in part by the National Institute of General Medical Sciences (NIGMS) of the National Institutes of Health (NIH) Maximizing Access to Research Careers T34 GM105549 grant to E.A.S. Use of BioCARS was supported by NIH NIGMS under grant number P41 GM118217. This research is partially supported by Platform Project for Supporting Drug Discovery and Life Science Research (Basis for Supporting Innovative Drug Discovery and Life Science Research) from the Japan Agency for Medical Research and Development under grant number JP20am0101070. Molecular graphics and analyses performed with UCSF Chimera, developed by the Resource for Biocomputing, Visualization, and Informatics at the University of California, San Francisco, with support from NIH P41-GM103311. We thank Takanori Nakane for assistance with data processing.

AUTHOR CONTRIBUTIONS

Conceptualization, E.A.S. and M.S.; Methodology, S.W., E.A.S., and M.S.; Samples, M.C., J.S., M.N., L.A., D.F., and E.A.S.; Data collection, M.C., S.P., J.S., M.N., I.P., L.A., T.N.M., E. C., W.Y.W., D.F., V.Ś., M.M., L.C., S.I., E.N., R.T., T.T., L.F., K.T., S.O., S.W., E.A.S., and M.S.; Data processing, I.P., L.C., and S.P.; Data analysis, S.P., E.A.S., and M.S.; Writing – original draft, E.A.S. and M.S. with input from all authors; Writing – review & editing, E.A.S., S.W., and M.S. with input from all authors.; Funding acquisition, S.I., S.W., E.A.S., and M.S.; Resources and supervision, S.I., S.W., E.A.S., and M.S..

DECLARATION OF INTERESTS

The authors declare no competing interests.

INCLUSION AND DIVERSITY

One or more of the authors of this paper self-identifies as an underrepresented ethnic minority in science. One or more of the authors of this paper received support from a program designed to increase minority representation in science.

Received: October 27, 2020
Revised: January 31, 2021
Accepted: March 2, 2021
Published: March 22, 2021

REFERENCES

Auldridge, M.E., and Forest, K.T. (2011). Bacterial phytochromes: more than meets the light. Crit. Rev. Biochem. Mol. *46*, 67–88.

Bai, Y., Rottwinkel, G., Feng, J., Liu, Y., and Lamparter, T. (2016). Bacteriophytochromes control conjugation in *Agrobacterium fabrum*. J. Photochem. Photobiol. B Biol. *161*, 192–199.

Barends, T.R., Foucar, L., Ardevol, A., Nass, K., Aquila, A., Botha, S., Doak, R.B., Falahati, K., Hartmann, E., Hilpert, M., et al. (2015). Direct observation of ultrafast collective motions in CO myoglobin upon ligand dissociation. Science *350*, 445–450.

Barkovits, K., Schubert, B., Heine, S., Scheer, M., and Frankenberg-Dinkel, N. (2011). Function of the bacteriophytochrome BphP in the RpoS/Las quorum-sensing network of Pseudomonas aeruginosa. Microbiology *157*, 1651–1664.

Barty, A., Kirian, R.A., Maia, F.R.N.C., Hantke, M., Yoon, C.H., White, T.A., and Chapman, H. (2014). Cheetah: software for high-throughput reduction and analysis of serial femtosecond X-ray diffraction data. J. Appl. Crystallogr. *47*, 1118–1131.

Batschauer, A. (1998). Photoreceptors of higher plants. Planta *206*, 479–492.

Berman, H.M., Battistuz, T., Bhat, T.N., Bluhm, W.F., Bourne, P.E., Burkhardt, K., Feng, Z., Gilliland, G.L., Iype, L., Jain, S., et al. (2002). The Protein Data Bank. Acta Crystallogr. D Biol. Crystallogr. *58*, 899–907.

Blumenstein, A., Vienken, K., Tasler, R., Purschwitz, J., Veith, D., Frankenberg-Dinkel, N., and Fischer, R. (2005). The *Aspergillus nidulans* phytochrome FphA represses sexual development in red light. Curr. Biol. *15*, 1833–1838.

Burgie, E.S., Zhang, J., and Vierstra, R.D. (2016). Crystal structure of *Deinococcus* phytochrome in the photoactivated state reveals a cascade of structural rearrangements during photoconversion. Structure *24*, 448–457.

Butler, W.L., Norris, K.H., Siegelman, H.W., and Hendricks, S.B. (1959). Detection, assay, and preliminary purification of the pigment controlling photoresponsive development of plants. Proc. Natl. Acad. Sci. U S A *89*, 1703–1708.

Cherry, J.R., Hondred, D., Walker, J.M., and Vierstra, R.D. (1992). Phytochrome requires the 6-kDa N-terminal domain for full biological activity. Proc. Natl. Acad. Sci. U S A *89*, 5039–5043.

Claesson, E., Wahlgren, W.Y., Takala, H., Pandey, S., Castillon, L., Kuznetsova, V., Henry, L., Panman, M., Carrillo, M., Kubel, J., et al. (2020). The primary structural photoresponse of phytochrome proteins captured by a femtosecond X-ray laser. eLife *9*, e53514.

Davis, S.J., Vener, A.V., and Vierstra, R.D. (1999). Bacteriophytochromes: phytochrome-like photoreceptors from nonphotosynthetic eubacteria. Science *286*, 2517–2520.

Emsley, P., Lohkamp, B., Scott, W.G., and Cowtan, K. (2010). Features and development of Coot. Acta Crystallogr. D Biol. Crystallogr. *66*, 486–501.

Essen, L.O., Mailliet, J., and Hughes, J. (2008). The structure of a complete phytochrome sensory module in the Pr ground state. Proc. Natl. Acad. Sci. U S A *105*, 14709–14714.

Fixen, K.R., Baker, A.W., Stojkovic, E.A., Beatty, J.T., and Harwood, C.S. (2014). Apo-bacteriophytochromes modulate bacterial photosynthesis in response to low light. Proc. Natl. Acad. Sci. U S A *111*, E237–E244.

Giraud, E., Fardoux, J., Fourrier, N., Hannibal, L., Genty, B., Bouyer, P., Dreyfus, B., and Vermeglio, A. (2002). Bacteriophytochrome controls photosystem synthesis in anoxygenic bacteria. Nature *417*, 202–205.

Giraud, E., Zappa, S., Vuillet, L., Adriano, J.M., Hannibal, L., Fardoux, J., Berthomieu, C., Bouyer, P., Pignol, D., and Vermeglio, A. (2005). A new type of bacteriophytochrome acts in tandem with a classical bacteriophytochrome to control the antennae synthesis in *Rhodopseudomonas palustris*. J. Biol. Chem. *280*, 32389–32397.

Gourinchas, G., Etzl, S., Gobl, C., Vide, U., Madl, T., and Winkler, A. (2017). Long-range allosteric signaling in red light-regulated diguanylyl cyclases. Sci. Adv. *3*, e1602498.

Gourinchas, G., Heintz, U., and Winkler, A. (2018). Asymmetric activation mechanism of a homodimeric red light-regulated photoreceptor. eLife *7*, e34815.

Grunbein, M.L., and Nass Kovacs, G. (2019). Sample delivery for serial crystallography at free-electron lasers and synchrotrons. Acta Crystallogr. D Struct. Biol. *75*, 178–191.

Grunbein, M.L., Stricker, M., Nass Kovacs, G., Kloos, M., Doak, R.B., Shoeman, R.L., Reinstein, J., Lecler, S., Haacke, S., and Schlichting, I. (2020). Illumination guidelines for ultrafast pump-probe experiments by serial femtosecond crystallography. Nat. Methods *17*, 681–684.

Gushchin, I., Melnikov, I., Polovinkin, V., Ishchenko, A., Yuzhakova, A., Buslaev, P., Bourenkov, G., Grudinin, S., Round, E., Balandin, T., et al. (2017). Mechanism of transmembrane signaling by sensor histidine kinases. Science *356*, eaah6345.

Gustavsson, E., Isaksson, L., Persson, C., Mayzel, M., Brath, U., Vrhovac, L., Ihalainen, J.A., Karlsson, B.G., Orekhov, V., and Westenhoff, S. (2020). Modulation of structural heterogeneity controls phytochrome photoswitching. Biophysical J. *118*, 415–421.

Henderson, R., and Moffat, K. (1971). The difference Fourier technique in protein crystallography: errors and their treatment. Acta Crystallogr. B *27*, 1414–1420.

Hughes, J., Lamparter, T., Mittmann, F., Hartmann, E., Gartner, W., Wilde, A., and Borner, T. (1997). A prokaryotic phytochrome. Nature *386*, 663.

Hutchison, C.D.M., Kaucikas, M., Tenboer, J., Kupitz, C., Moffat, K., Schmidt, M., and van Thor, J.J. (2016). Photocycle populations with femtosecond excitation of crystalline photoactive yellow protein. Chem. Phys. Lett. *654*, 63–71.

Isaksson, L., Gustavsson, E., Persson, C., Brath, U., Vrhovac, L., Karlsson, G., Orekhov, V., and Westenhoff, S. (2020). Signaling mechanism of phytochromes in solution. Structure *29*, 151–160.e3.

Jiang, Z., Swem, L.R., Rushing, B.G., Devanathan, S., Tollin, G., and Bauer, C.E. (1999). Bacterial photoreceptor with similarity to photoactive yellow protein and plant phytochromes. Science *285*, 406–409.

Jung, Y.O., Lee, J.H., Kim, J., Schmidt, M., Moffat, K., Srajer, V., and Ihee, H. (2013). Volume-conserving trans-cis isomerization pathways in photoactive yellow protein visualized by picosecond X-ray crystallography. Nat. Chem. *5*, 212–220.

Kameshima, T., Ono, S., Kudo, T., Ozaki, K., Kirihara, Y., Kobayashi, K., Inubushi, Y., Yabashi, M., Horigome, T., Holland, A., et al. (2014). Development of an X-ray pixel detector with multi-port charge-coupled device for X-ray free-electron laser experiments. Rev. Scientific Instr. *85*, 033110.

Kubo, M., Nango, E., Tono, K., Kimura, T., Owada, S., Song, C.Y., Mafune, F., Miyajima, K., Takeda, Y., Kohno, J., et al. (2017). Nanosecond pump-probe device for time-resolved serial femtosecond crystallography developed at SACLA. J. Synchrotron Radiat. *24*, 1086–1091.

Legris, M., Ince, Y.C., and Fankhauser, C. (2019). Molecular mechanisms underlying phytochrome-controlled morphogenesis in plants. Nat. Commun. *10*, 5219.

Mathes, T., Ravensbergen, J., Kloz, M., Gleichmann, T., Gallagher, K.D., Woitowich, N.C., St. Peter, R., Kovaleva, S.E., Stojkovic, E., and Kennis, J.T.M. (2014). Femto- to microsecond photodynamics of an unusual bacteriophytochrome. J. Phys. Chem. Lett. *6*, 239–243.

McGrane, R., and Beattie, G.A. (2017). *Pseudomonas syringae* pv. *syringae* B728a regulates multiple stages of plant colonization via the bacteriophytochrome BphP1. MBio *8*, https://doi.org/10.1128/mBio.01178-17.

Murshudov, G.N., Skubak, P., Lebedev, A.A., Pannu, N.S., Steiner, R.A., Nicholls, R.A., Winn, M.D., Long, F., and Vagin, A.A. (2011). REFMAC5 for the refinement of macromolecular crystal structures. Acta Crystallogr. D Biol. Crystallogr. *67*, 355–367.

Nakane, T., Joti, Y., Tono, K., Yabashi, M., Nango, E., Iwata, S., Ishitani, R., and Nureki, O. (2016). Data processing pipeline for serial femtosecond crystallography at SACLA. J. Appl. Crystallogr. *49*, 1035–1041.

Nango, E., Royant, A., Kubo, M., Nakane, T., Wickstrand, C., Kimura, T., Tanaka, T., Tono, K., Song, C.Y., Tanaka, R., et al. (2016). A three-dimensional movie of structural changes in bacteriorhodopsin. Science *354*, 1552–1557.

Nogales, E. (2016). The development of cryo-EM into a mainstream structural biology technique. Nat. Methods *13*, 24–27.

Nogly, P., Weinert, T., James, D., Carbajo, S., Ozerov, D., Furrer, A., Gashi, D., Borin, V., Skopintsev, P., Jaeger, K., et al. (2018). Retinal isomerization in bacteriorhodopsin captured by a femtosecond x-ray laser. Science *361*, https://doi.org/10.1126/science.aat0094.

Otero, L.H., Klinke, S., Rinaldi, J., Velazquez-Escobar, F., Mroginski, M.A., Fernandez Lopez, M., Malamud, F., Vojnov, A.A., Hildebrandt, P., Goldbaum, F.A., et al. (2016). Structure of the full-length bacteriophytochrome from the plant pathogen *Xanthomonas campestris* provides clues to its long-range signaling mechanism. J. Mol. Biol. *428*, 3702–3720.

Pande, K., Hutchison, C.D.M., Groenhof, G., Aquila, A., Robinson, J.S., Tenboer, J., Basu, S., Boutet, S., Deponte, D., Liang, M., et al. (2016). Femtosecond structural dynamics drives the trans/cis isomerization in photoactive yellow protein. Science *352*, 725–729.

Pandey, S., Bean, R., Sato, T., Poudyal, I., Bielecki, J., Cruz Villarreal, J., Yefanov, O., Mariani, V., White, T.A., Kupitz, C., et al. (2020). Time-resolved serial femtosecond crystallography at the European XFEL. Nat. Methods *17*, 73–78.

Pettersen, E.F., Goddard, T.D., Huang, C.C., Couch, G.S., Greenblatt, D.M., Meng, E.C., and Ferrin, T.E. (2004). UCSF chimera—a visualization system for exploratory research and analysis. J. Comput. Chem. *25*, 1605–1612.

Poudyal, I., Schmidt, M., and Schwander, P. (2020). Single-particle imaging by x-ray free-electron lasers—how many snapshots are needed? Struct. Dyn. *7*, 024102.

Roessler, C.G., Agarwal, R., Allaire, M., Alonso-Mori, R., Andi, B., Bachega, J.F., Bommer, M., Brewster, A.S., Browne, M.C., Chatterjee, R., et al. (2016). Acoustic injectors for drop-on-demand serial femtosecond crystallography. Structure *24*, 631–640.

Sanchez, J.C., Carrillo, M., Pandey, S., Noda, M., Aldama, L., Feliz, D., Claesson, E., Wahlgren, W.Y., Tracy, G., Duong, P., et al. (2019). High-resolution crystal structures of amyxobacterial phytochrome at cryo and room temperatures. Struct. Dyn. *6*, 054701.

Schmidt, M. (2019). Time-resolved macromolecular crystallography at pulsed X-ray sources. Int. J. Mol. Sci. *20*, 1401.

Schmidt, M., Nienhaus, K., Pahl, R., Krasselt, A., Anderson, S., Parak, F., Nienhaus, G.U., and Srajer, V. (2005). Ligand migration pathway and protein dynamics in myoglobin: a time-resolved crystallographic study on L29W MbCO. Proc. Natl. Acad. Sci. U S A *102*, 11704–11709.

Schmidt, M., Patel, A., Zhao, Y., and Reuter, W. (2007). Structural basis for the photochemistry of alpha-phycoerythrocyanin. Biochemistry *46*, 416–423.

Shimazu, Y., Tono, K., Tanaka, T., Yamanaka, Y., Nakane, T., Mori, C., Kimura, K.T., Fujiwara, T., Sugahara, M., Tanaka, R., et al. (2019). High-viscosity sample-injection device for serial femtosecond crystallography at atmospheric pressure. J. Appl. Crystallogr. *52*, 1280–1288.

Shu, X., Royant, A., Lin, M.Z., Aguilera, T.A., Lev-Ram, V., Steinbach, P.A., and Tsien, R.Y. (2009). Mammalian expression of infrared fluorescent proteins engineered from a bacterial phytochrome. Science *324*, 804–807.

Skopintsev, P., Ehrenberg, D., Weinert, T., James, D., Kar, R.K., Johnson, P.J.M., Ozerov, D., Furrer, A., Martiel, I., Dworkowski, F., et al. (2020). Femtosecond-to-millisecond structural changes in a light-driven sodium pump. Nature *583*, 314–318.

Speziale, S., Jiang, F., Caylor, C.L., Kriminski, S., Zha, C.S., Thorne, R.E., and Duffy, T.S. (2003). Sound velocity and elasticity of tetragonal lysozyme crystals by Brillouin spectroscopy. Biophys. J. *85*, 3202–3213.

Srajer, V., Crosson, S., Schmidt, M., Key, J., Schotte, F., Anderson, S., Perman, B., Ren, Z., Teng, T.Y., Bourgeois, D., et al. (2000). Extraction of accurate structure-factor amplitudes from Laue data: wavelength normalization with wiggler and undulator X-ray sources. J. Synchrotron Radiat. *7*, 236–244.

Srajer, V., Ren, Z., Teng, T.Y., Schmidt, M., Ursby, T., Bourgeois, D., Pradervand, C., Schildkamp, W., Wulff, M., and Moffat, K. (2001). Protein conformational relaxation and ligand migration in myoglobin: a nanosecond to millisecond molecular movie from time-resolved Laue X-ray diffraction. Biochemistry *40*, 13802–13815.

Srajer, V., Teng, T.Y., Ursby, T., Pradervand, C., Ren, Z., Adachi, S., Schildkamp, W., Bourgeois, D., Wulff, M., and Moffat, K. (1996). Photolysis of the carbon monoxide complex of myoglobin: nanosecond time-resolved crystallography. Science *274*, 1726–1729.

Sugahara, M., Mizohata, E., Nango, E., Suzuki, M., Tanaka, T., Masudala, T., Tanaka, R., Shimamura, T., Tanaka, Y., Suno, C., et al. (2015). Grease matrix as a versatile carrier of proteins for serial crystallography. Nat. Methods *12*, 61–63.

Sugahara, M., Nakane, T., Masuda, T., Suzuki, M., Inoue, S., Song, C., Tanaka, R., Nakatsu, T., Mizohata, E., Yumoto, F., et al. (2017). Hydroxyethyl cellulose matrix applied to serial crystallography. Sci. Rep. *7*, 703.

Takala, H., Bjorling, A., Berntsson, O., Lehtivuori, H., Niebling, S., Hoernke, M., Kosheleva, I., Henning, R., Menzel, A., Ihalainen, J.A., et al. (2014). Signal amplification and transduction in phytochrome photosensors. Nature *509*, 245–248.

Takala, H., Edlund, P., Ihalainen, J.A., and Westenhoff, S. (2020). Tips and turns of bacteriophytochrome photoactivation. Photochem. Photobiol. Sci. *19*, 1488–1510.

Tenboer, J., Basu, S., Zatsepin, N., Pande, K., Milathianaki, D., Frank, M., Hunter, M., Boutet, S., Williams, G.J., Koglin, J.E., et al. (2014). Time-resolved serial crystallography captures high-resolution intermediates of photoactive yellow protein. Science *346*, 1242–1246.

Toh, K.C., Stojkovic, E.A., van Stokkum, I.H., Moffat, K., and Kennis, J.T. (2010). Proton-transfer and hydrogen-bond interactions determine

fluorescence quantum yield and photochemical efficiency of bacteriophytochrome. Proc. Natl. Acad. Sci. U S A *107*, 9170–9175.

Toh, K.C., Stojkovic, E.A., van Stokkum, I.H.M., Moffat, K., and Kennis, J.T. (2011a). The photochemistry of bacteriophytochrome: key to its use as a deep-tissue fluorescence probe. Biophys. J. *100*, https://doi.org/10.1016/j.bpj.2010.12.1174.

Toh, K.C., Stojkovic, E.A., van Stokkum, I.H.M., Moffat, K., and Kennis, J.T.M. (2011b). Fluorescence quantum yield and photochemistry of bacteriophytochrome constructs. Phys. Chem. Chem. Phys. *13*, 11985–11997.

Wagner, J.R., Brunzelle, J.S., Forest, K.T., and Vierstra, R.D. (2005). A light-sensing knot revealed by the structure of the chromophore-binding domain of phytochrome. Nature *438*, 325–331.

White, T.A., Mariani, V., Brehm, W., Yefanov, O., Barty, A., Beyerlein, K.R., Chervinskii, F., Galli, L., Gati, C., Nakane, T., et al. (2016). Recent developments in CrystFEL. J. Appl. Crystallogr. *49*, 680–689.

Winn, M.D., Ballard, C.C., Cowtan, K.D., Dodson, E.J., Emsley, P., Evans, P.R., Keegan, R.M., Krissinel, E.B., Leslie, A.G.W., McCoy, A., et al. (2011). Overview of the CCP4 suite and current developments. Acta Crystallogr. D *67*, 235–242.

Woitowich, N.C., Halavaty, A.S., Waltz, P., Kupitz, C., Valera, J., Tracy, G., Gallagher, K.D., Claesson, E., Nakane, T., Pandey, S., et al. (2018). Structural basis for light control of cell development revealed by crystal structures of a myxobacterial phytochrome. IUCrJ *5*, 619–634.

Yang, X., Kuk, J., and Moffat, K. (2008). Crystal structure of *Pseudomonas aeruginosa* bacteriophytochrome: photoconversion and signal transduction. Proc. Natl. Acad. Sci. U S A *105*, 14715–14720.

Yang, X., Ren, Z., Kuk, J., and Moffat, K. (2011). Temperature-scan cryocrystallography reveals reaction intermediates in bacteriophytochrome. Nature *479*, 428–432.

Yang, X., Stojkovic, E.A., Kuk, J., and Moffat, K. (2007). Crystal structure of the chromophore binding domain of an unusual bacteriophytochrome, RpBphP3, reveals residues that modulate photoconversion. Proc. Natl. Acad. Sci. U S A *104*, 12571–12576.

Yang, X., Stojkovic, E.A., Ozarowski, W.B., Kuk, J., Davydova, E., and Moffat, K. (2015). Light signaling mechanism of two tandem bacteriophytochromes. Structure *23*, 1179–1189.

Yeh, K.C., Wu, S.H., Murphy, J.T., and Lagarias, J.C. (1997). A cyanobacterial phytochrome two-component light sensory system. Science *277*, 1505–1508.

STAR★METHODS

KEY RESOURCES TABLE

REAGENT or RESOURCE	SOURCE	IDENTIFIER
Bacterial and Virus Strains		
E. coli BL21(DE3) competent cells	New England Biolabs	Cat# C2527I
Chemicals, Peptides, and Recombinant Proteins		
Recombinant SaBphP2, aa 1 – 489	(Sanchez et al., 2019)	N/A
50% w/v PEG 4000	Hampton Research	HR2-529
20% w/v Benzamidine Hydrochloride	Hampton Research	HR2-428-69
1M Sodium citrate tribasic dihydrate pH 5.6	Hampton Research	HR2-935-15
Nuclear grade grease	Super Lube	42150
Deposited Data		
SaBphP2 PCM structure 5 ns after laser excitation	This paper	PDB: 7JR5
SaBphP2 PCM structure 33 ms after laser excitation	This paper	PDB: 7JRI
SaBphP2 PCM structure, reference in the dark	(Sanchez et al., 2019)	PDB: 6PTQ
Recombinant DNA		
pET28c-SaBphP2 PCM (1-489aa)	(Sanchez et al., 2019)	N/A
Software and Algorithms		
Data processing pipeline at SACLA	(Nakane et al., 2016)	
Cheetah	(Barty et al., 2014)	https://github.com/biochem-fan/
CrystFEL	(White et al., 2016)	https://github.com/biochem-fan/
Structural Modeling: Coot	(Emsley et al., 2010)	https://www.ccp4.ac.uk/
Structural Refinement: Refmac	(Murshudov et al., 2011)	https://www.ccp4.ac.uk/
Pearson Correlation Coefficient, pcc.f	This paper	Available from lead contact
UCSF chimera	(Pettersen et al., 2004)	https://www.cgl.ucsf.edu/chimera/
Other		
TALON® Metal Affinity Resin	Takara Bio	Cat# 635503
Amicon Ultra Centrifugal Filters	Millipore Sigma	Cat# UFC901024

RESOURCE AVAILABLITY

Lead contact

Further information and requests for resources and reagents should be directed to and will be fulfilled by the Lead Contact, Marius Schmidt (smarius@uwm.edu).

Materials availability

The SaBphP2 PCM expression system is available from the Lead Contact upon request.

Data and code availability

Structural models as well as structure factor amplitudes were deposited in the Protein Data Bank, Research Collaboratory for Structure Bioinformatics (RCSB PDB, rcsb.org) with accession codes PDB: 7JR5 and PDB: 7JRI for the wild-type 5ns and 33 ms structures of *Sa*BphP2 PCM, respectively. Code to produce difference maps and extrapolated maps is available from the Lead Contact upon request.

EXPERIMENTAL MODEL AND SUBJECT DETAILS

Recombinant protein was produced in a pET28c vector (Novagen) and co-expressed with heme oxygenase from plasmid pET11a in E. coli BL21(DE3) cells (New England Biolabs) as described by Sanchez et al., (2019). Frozen stock of BL21(DE3) cells with respective

expression plasmids was suspended in 50 mL LB broth with 100 μg/ml ampicillin at 37°C overnight and used for protein expression. Cells were grown at 37°C to 3 x 10^8 cells/mL and induced at 18°C for 16 – 18 hours using 1 mmol/L isopropyl-β-thiogalactopyranoside (IPTG) and 0.5 mmol/L δ-aminolevulinic acid.

METHOD DETAILS

Protein purification and crystallization

Cells were harvested and protein purified as outlined by Sanchez et al., (2019). Cells were recovered in 150 mM NaCl, 20 mM Tris-HCl pH 8.0 and 15% v/v glycerol with protease inhibitor (Roche). After cell lysis by sonication and centrifugation at 25,000 g for 1 h at 4°C, 20 μM biliverdin stock in DMSO was added to the supernatant (1:100) for 15 min at 4°C. The solution was applied to Talon Co^{+2} metal ion affinity chromatography columns (Takara Clontech). The *Sa*BphP2-PCM was eluted by 300 mM imidazole, 20 mM NaCl and 20 mM Tris-HCl pH 8.0. Buffer exchange and concentration was achieved by Amicon filtration units (10 kDa cutoff) at 4000 rpm. Microcrystals of the *Sa*BphP2-PCM were grown as described (Sanchez et al., 2019) by mixing a mother liquor consisting of 0.17 M Ammonium acetate, 0.085 M Sodium citrate tribasic dihydrate pH 5.6, 25.5% w/v Polyethylene glycol 4000, 15% v/v Glycerol (cryo-screen solution) and 3% w/v Benzamidine Hydrochloride, with 60 mg/mL protein (3:2 protein to mother liquor ratio). The mixture was seeded with finely crushed macrocrystals. After 4 days, the microcrystals were collected and concentrated to about 10^{11} crystals /ml and subsequently folded into a ten-fold amount of nuclear grade grease (Sugahara et al., 2015, 2017). All steps in crystallization and tray observations were performed under green safety light.

Experimental design

Pump-probe experiments were conducted at beamline BL2 at SACLA using a nanosecond laser (Kubo et al., 2017; Nango et al., 2016). For our nanosecond TR-SFX experiments, a two-sided laser illumination geometry was used, where a split laser beam intercepts the X-rays and the viscous jet (Figure 3). A relatively large laser fluence of 3.5 mJ/mm^2 was chosen for each side, respectively. The laser fluence was chosen based on absorption measurements on grease crystal mixtures (Figure S3). For femtosecond TR-SFX experiments X-rays and laser illumination are parallel (Barends et al., 2015; Claesson et al., 2020; Grunbein and Nass Kovacs, 2019; Grunbein et al., 2020; Nogly et al., 2018; Pande et al., 2016). Then, the effective 'hit-rate' of the laser illumination is equivalent to the X-ray hit-rate (Grunbein and Nass Kovacs, 2019; Grunbein et al., 2020) and shading by other crystals in the viscous jet does not play a role. This has consequences for the selection of the laser fluence, especially for fs laser illumination, which are discussed (Grunbein and Nass Kovacs, 2019; Grunbein et al., 2020). In contrast, for a perpendicular geometry as employed here, the entire path of the X-ray beam through the crystal must be illuminated by the laser. This leads to an effective laser beam size that is much larger than the X-ray beam (Figure 3B). The large effective laser beam size is likely intercepted by other crystals in the relatively thick (100 μm) viscous jet. This results in substantial shading by crystals not exposed to the X-rays. To roughly estimate this shading, the crystal-grease mixtures were sandwiched between cover slides kept apart by 50 μm washers to match the optical path through half of the 100 μm thick viscous jet. Absorption was measured with a microscopectrophotometer located at BioCARS (APS, Argonne National Laboratory). Grease mixed with *Sa*BphP2 PCM microcrystals shows an absorption of 0.75 at 640 nm (Figure S3), which corresponds to a 5 fold reduction of the incident fluence. In addition, at 640 nm the absorption is only 40% of that at the maximum at 700 nm. Accordingly, a 3.5 mJ/mm^2 fluence at 640 nm is equivalent to only about 0.28 mJ/mm^2 at the absorption maximum. Because of the 2-sided illumination the total fluence at a crystal probed in the middle of the jet is 0.56 mJ/mm^2 (with reference to the absorption maximum). Given the previous experiences with photoactive yellow protein (Pande et al., 2016; Tenboer et al., 2014), 0.56 mJ/mm^2 is well below the threshold to generate damage even with femtosecond laser pulses (Hutchison et al., 2016), and does not play any adverse role with nanosecond laser pulses. We believe that for our experimental geometry strong laser excitation has been essential to boost excitation levels to the extent that analyzable signal is obtained.

TR-SFX data acquisition and processing

200 μl of the crystal-grease mixture were transferred into an injector reservoir (Shimazu et al., 2019) and extruded into air at ambient temperatures (293 K) through a 100 μm wide nozzle with a flow rate of about 4 μl/min. The photoreaction was started with 5 ns lasers pulses of 640 nm wavelength with a full width half maximum (FWHM) of 52 μm. The laser repetition rate was varied between 15 Hz and 10 Hz (Figures 3C and 3D). A flow rate of 4 μl/min displaces at least a 300 μm column of grease between the high frequency (15 Hz) laser pulses. 5 ns after the laser pulse the stream of microcrystals was exposed in air to intense X-ray pulses (λ = 1.38 Å) of <10 fs duration. The scattering background was minimized by using a helium-purged collimator. We used a pump-probe, dark 1 (33 ms), dark 2 (66 ms) (Figure 3B) data collection strategy to assess whether a once laser illuminated/excited viscous jet volume has left the X-ray interaction region and moved sufficiently that multiple laser excitations of the X-ray probed volume are avoided.

For all experiments, diffraction patterns were collected on a CCD detector with eight modules (Kameshima et al., 2014) and analyzed with a user-friendly data-processing pipeline (Nakane et al., 2016) consisting of hit-finding with Cheetah (Barty et al., 2014), and indexing and Monte Carlo integration by CrystFEL (White et al., 2016). Reference SFX data have been collected previously at SACLA without laser excitation (Sanchez et al., 2019). The reference structure is available from the protein data bank (Berman et al., 2002) with entry 6PTQ. The reference SFX data were quickly reprocessed to 2.1 Å (Table 1). For all datasets the hit rate was about 30%. About 50% of diffraction patterns were successfully indexed. The extracted partial intensities were merged to full reflection

intensities using the 'partialator' program in CrystFEL. For data statistics, see Table 1. The full intensities were converted to structure-factor amplitudes by software based on the CCP4 suite of programs (Winn et al., 2011).

Computation of difference electron density maps

Weighted difference electron density (DED) maps were calculated from the TR-SFX data and the reference data as described (Schmidt, 2019; Tenboer et al., 2014). The DED maps at 33 ms and 66 ms were inspected for strong DED features near the chromophore. At 33 ms clear signal is present (Figures S2B). At 66 ms, only spurious and randomly distributed features could be detected (Figure S2 C). This demonstrates that the viscous jet is extruded fast enough to cope with a data collection strategy shown in Figure 3C (pump-probe, dark) as with this strategy the next laser pulses arrives 66 ms after the previous one. This way, the laser excites a pristine jet volume that is free from contaminations from earlier laser pulses. Data for two time-delays are collected from the same experimental setup, as the first X-ray pulse after laser excitation contributes diffraction patterns for a 5 ns dataset, the second X-ray pulse contributes to a 33 ms dataset. Needless to say, when only one intermittent X-ray pulse is used, the reference data must be collected separately with the laser switched off (see above).

Structure determination

Structural models were derived from extrapolated maps calculated by adding N*DF to the structure factors calculated from an accurately refined dark state *Sa*BphP2 PCM model. The factor N_C required to extrapolate the fraction of excited molecules to 100% was determined by integrating negative density in the extrapolated maps until the values diverge (Pandey et al., 2020). For the 5 ns time delay N_C is 19 (Figure S4A) which corresponds to a population of 10.5% activated molecules in the crystal (Schmidt, 2019). For the 33 ms time delay N_C is 22 (Figure S4B), about 9% of molecules are activated. The chromophore was moved by hand into the extrapolated maps calculated at 5 ns and 33 ms time delays. The D-ring was rotated about the double bond Δ15,16 to achieve maximum agreement with the DED maps as well as with the extrapolated density. Multiple D-ring orientations were accommodated by generating chromophore double conformations with the the program 'coot' (Emsley et al., 2010). The apo-SaBphP2 PCM structures at 5 ns and 33 ms pump-probe delays were determined by using the real space (stepped) refinement option in 'coot'. This was followed by a scripted 'zoned' refinement, also performed in real space in 'coot'. For this, the script activates α-helical and β-strain restraints when needed. After the real space refinement the agreement with the difference map was inspected, and if necessary corrected further by hand. Double conformations for certain residues (His275, Tyr 248) were introduced to accommodate DED features that result from the various D-ring orientations. If in doubt, extrapolated maps with higher N ($N \sim 40$) were computed to verify the presence or to clarify the absence of individual structural moieties at specific locations in space. A final reciprocal space refinement was conducted with refmac5v.7.0 (Murshudov et al., 2011) using phased extrapolated structure factors (PESF) calculated as described previously (Claesson et al., 2020; Pandey et al., 2020; Schmidt, 2019). As calculated structure factors of the reference structure are used to determine the PESFs, the final refinement is biased towards the reference (dark) structure. Therefore, refined differences are (i) real, and (ii) sometimes tend to be underdetermined by a fraction of an Å. Extrapolated amplitudes also amplify errors in the difference amplitudes N_c times. Due to this, structures were refined to 2.4 Å which is lower than the resolution limit of the data. Due to the same reasons, occupancies for the chromophore and other amino acid residues double conformations were not refined. Occupancies were rather distributed on equal par among the double conformations.

Pearson correlation for Ring-D orientation

Once a model that interprets the DED is determined, calculated DED maps can be computed from this model and the reference model (Claesson et al., 2020; Pandey et al., 2020) by subtracting structure factors calculated from both models. In order to corroborate the assessment of clockwise and counter-clockwise D-ring rotation, the Pearson Correlation Coefficient was used. For the correlation coefficient the observed and calculated DED maps are compared. Since negative DED is always on top of the reference model, the negative DED does not add information to distinguish competing models. Accordingly, only positive DED features near the ring-D region are compared. A Fortran program ('pcc.f') was developed that reads difference maps in ccp4 format, masks out specific volumes around a pdb-file provided to the program, and calculates the Pearson correlation coefficient (PCC) within this masked volume. Here, the mask volume is determined by the coordinates of the D-ring in both clockwise and counter-clockwise orientations. Within this volume, the PCC was determined by a grid-wise comparison of positive observed and corresponding calculated DED features as:

$$PCC = \frac{\sum_i (\Delta\rho^{obs} - \langle\Delta\rho^{obs}\rangle)(\Delta\rho^{calc} - \langle\Delta\rho^{calc}\rangle)}{\sqrt{\sum_i (\Delta\rho^{obs} - \langle\Delta\rho^{obs}\rangle)^2}\sqrt{\sum_i (\Delta\rho^{calc} - \langle\Delta\rho^{calc}\rangle)^2}}.$$

The terms in the bracket are the averages computed from all grid points i in the mask. Although the average DED in an entire difference map is zero, the averages computed here are not zero, since only positive features are evaluated. In addition, map grid points i were selected only when the observed DED values are larger than a certain sigma value. With this, the PCC can be plotted as a function of increasing sigma values. In subunit A, at 5 ns, only the clockwise rotation is supported in particular by high DED features (Figure S4C). In subunit B, the PCC is similar regardless whether a model with a clockwise, a counter-clockwise or a double conformation is examined (Figure S4D). This demonstrates that both clockwise and counter-clockwise ring-D rotations produce

calculated DED features that explain the observed density equally well. The PCC cannot distinguish between the two ring-D orientations.

Detailed views of structural moieties

Structural views were generated with UCSF Chimera (Pettersen et al., 2004).

QUANTIFICATION AND STATISTICAL ANALYSIS

Statistical analysis of DED features

The signal content and signal variance (sigma values) in the DED maps were analyzed by histograms. Gaussian fits to the histogram should reproduce the root mean square deviation (RMSD) values of the fft program that calculates the DED when the signal is purely random. When the signal is weak and localized, it only changes the distribution in the flanks of the Gaussian (Srajer et al., 2000), but not the sigma value. If the signal is strong and everywhere, the fitted Gaussian becomes broader and does not fit the flanks. The noise originates from the experimental error in the difference amplitudes and errors introduced by the Fourier approximation (Henderson and Moffat, 1971). In the presence of localized signal, the noise and not the signal determines the sigma value of a DED map (Srajer et al., 2000). Here, this is not the case. In Figures 3C, a histogram of DED values derived from difference amplitudes $\Delta F = F_{66ms}-F_{Dark}$ is shown. The histogram is fit by a Gaussian with a sigma of 0.0125 $e^-/Å^3$. The same value is also reported by the fast Fourier program ('fft') from the ccp4 suite of programs. The Gaussian fits the histogram perfectly which outlines the random nature of the DED features. A histogram prepared from the 5ns-F_{dark} DED_{5ns} map is shown in Figure 3B. The Gaussian is broader than in Figure 3C, and the flanks of the histogram are not fit properly by the Gaussian. If the DED features containing signal would be sparse, the sigma from the fit would be essentially identical to the value obtained from the 66 ms control data only. However, it is larger, 0.0144 $e^-/Å^3$. The form of the histogram is an indication of strong signal throughout the map. For the DED_{5ns} map the sigma value is determined by all of the noise sources described above plus the signal. Consequently, for meaningful comparisons, the DED_{5ns} map must be contoured as a multiple of the sigma value found in the DED_{66ms} control map, as this reflects the error level in a DED map without signal.

As large numbers of DED features were found, it is useful to estimate how many of these features might be generated by the noise sources mentioned above. For this, DED maps were sampled on a 3D grid no larger than $2(h_{max}+1)$with h_{max} the maximum h,k and l values within the resolution limit. As an example: at a resolution of 2 Å and a unit cell axis a = 80 Å, h_{max} is 40. Assuming similar values for the other cell axes, the unit cell and its DED content is sampled on a 82 x 82 x 82 grid. This way the DED peaks found in such a map correspond to independent features. Table 2 contrasts the number of DED features observed at 33 ms to the ones expected to occur randomly in the DED map. On the 3 sigma level, for example, 1839 features are expected to be purely random, and 3167 features are observed. On the 5 sigma level, the probability of a feature to be random is so low that not even one feature is expected in the entire DED map, yet 264 features (132 for a *Sa*BphP2 PCM dimer located in the asymmetric unit) are observed. To bring this into perspective, in the strong difference map determined for the photoactive yellow protein at a 3 ps pump-probe time delay (Pande et al., 2016), only 12 5-sigma features, two per symmetry related PYP molecule, are observed (at 2.1 Å resolution to be compatible with the resolution achieved here, and h_{max} determined as described).